Journal of Biomedical Optics 10(6), 064038 (November/December 2005)

Fast three-dimensional laser scanning scheme using acousto-optic deflectors

Gaddum Duemani Reddy
Rice University
Department of Bioengineering
Houston, Texas 77005

Peter Saggau
Baylor College of Medicine
Department of Neuroscience
Houston, Texas 77030
E-mail: psaggau@bcm.tmc.edu

Abstract. A scheme for fast 3-D laser scanning using acousto-optic deflectors is proposed and demonstrated. By employing counter-propagating acoustic waves that are both chirped and offset in their frequencies, we show that it is possible to simultaneously scan both axially and laterally with frame rates on the order of tens of kilohertz. This scheme was specifically designed for application with multiphoton imaging, particularly of neurons, where it will enable the concurrent monitoring of physiological signals at multiple locations within a microscopic 3-D volume ($350 \times 350 \times 200\ \mu\text{m}$). When used for this purpose, we demonstrate how this scheme would also inherently compensate for spatial dispersion when ultrafast laser pulses are used in acousto-optic multiphoton microscopy. [DOI: 10.1117/1.2141504]

Keywords: acousto-optic; multiphoton microscopy; three-dimensional; laser scanning; dispersion compensation.

Paper 05132R received Jun. 6, 2005; revised manuscript received Aug. 17, 2005; accepted for publication Aug. 17, 2005; published online Dec. 27, 2005. This paper is a revision of a paper presented at the SPIE conference on Multiphoton Microscopy in the Biomedical Sciences V, Jan. 2005, San Jose, California. The paper presented there appears (unrefereed) in SPIE Procedings Vol. 5700.

1 Introduction

Multiphoton laser scanning microscopy (MPLSM) has revolutionized fluorescence imaging in the field of biology by enhancing the quality of images obtained from optically thick tissue.[1] Some of the most productive applications of MPLSM have been in the field of experimental neuroscience, where it has been used to study neurodegenerative diseases,[2,3] synaptic plasticity,[4] and neuronal integration[4,5] in optically scattering live brain tissue. While the inherent sectioning ability, in combination with low levels of photodamage, provided by MPLSM has made it extremely useful for the structural imaging of small processes (e.g., dendritic spines $\sim 1\ \mu\text{m}$) deep within neuronal tissues,[5–7] the low temporal resolution available in most commercial MPLSM systems has limited its applicability in functional imaging to studies that involve only a few sites of interest. This is mainly because the maximum speed of the commonly used galvanometer-based method of laser scanning is inherently limited by inertia. Therefore, to achieve the sampling speeds necessary for monitoring physiological signals such as intracellular calcium dynamics, users typically restrict their scan region to a single line.[6,7] This not only significantly reduces the ability to accurately track physiological signals in complex-shaped cells such as neurons, but also prevents the monitoring of signals from more than just a few sites of interest along a neuron.

To overcome this limitation, our lab has combined the enhanced image quality provided by multiple advanced imaging techniques, including MPLSM (Ref. 8), with the enhanced temporal resolution and scanning flexibility of acousto-optic deflectors (AODs) to enhance the study of neurophysiological processes.[8–10] AODs utilize high-frequency sound waves that are propagated in an acousto-optic (AO) medium as a tunable diffraction grating.[11,12] Adjusting the frequency of the sound wave changes the diffraction angle and results in inertia-free beam deflection. By utilizing this property of AODs, we have been able to lower transition times between sites on a specimen to values in the low microsecond range ($\sim 20\ \mu\text{s}$) and remove any limit to the dwell time at a site. AODs have also enabled us to sample from any site in the specimen plane with the same transition time. As a result, we have been able to effectively monitor calcium transients along extensive regions of a neuron located deep in optically thick brain slices,[8] a task that cannot be performed with available commercial galvanometer-based confocal or multiphoton systems.

However, despite these enhancements in temporal resolution, our ability to effectively monitor signals at physiological speeds is limited to two-dimensional (2-D) scans. This is because the inertia-free beam-steering properties of AODs have thus far been applied only to lateral scanning, while the axial position of the focus is adjusted by the same mechanism available in most commercial systems, i.e., raising or lowering the objective lens with an actuator. This moves the back focal aperture of the objective lens, and since the focal length of the objective lens remains constant, also moves the axial position of the focus by the same amount. Thus, the axial speed of laser scanning is inherently limited by the inertia of the objective lens and its actuator. Consequently, the highest speed at which the axial position of the focus can be moved, even with the fastest available commercial equipment that we

---

Address all correspondence to Peter Saggau, Baylor College of Medicine, Department of Neuroscience, One Baylor Plaza, S730, Houston, TX 77030. Tel: 713–798–5082. Fax: 713–798–3946. E-mail: psaggau@bcm.tmc.edu

1083-3668/2005/10(6)/064038/10/$22.00 © 2005 SPIE

are aware of (pizeoactuators ~10 ms per step), is still orders of magnitudes slower than the speed at which we are able to move the lateral position of the focus. This inability to effectively monitor physiological signals in three dimensions is a serious constraint in neuroscience, since neurons are complex three-dimensional (3-D) structures[13] and develop in 3-D networks.[14]

Different methods have been proposed that would allow for laser scanning in the axial dimension. One of the most developed is the variable focal-length liquid-filled lens.[15–17] The principal mechanism for changing the focal length within this type of lens relies on changing the pressure within a lens chamber, which in turn deforms an elastic membrane and changes the curvature of the lens.[15] Recent developments have increased the maximum numerical aperature[16] and the speed[17] at which the focal position can be changed, but despite these improvements, the fastest variable focal length liquid-filled lenses that we are aware of still require at least one millisecond to change the focal position, which is 50 times longer than our current lateral transition time with AODs. Variable focal length lenses that use nematic liquid crystals[18–20] or electro-optic materials[21] to change the refractive index of the lens rather than the shape have also been developed. In general, for these types of lenses, generating fast response times requires restricting the thickness of the lens cell, which in turn severely limits the maximum change in focal length. Other mechanisms for variably adjusting focal length include using a deformable mirror,[22] however, this method also requires at least a millisecond to change the focal position and therefore is not suitable for applications that require frame rates greater than 1 kHz.

In this paper, we develop a 3-D scheme, proposed in a conference proceedings,[23] that uses four AODs together with a commercial objective lens to deterministically and quickly ($\sim 30\,\mu$s) position the focus spot in a microscopic 3-D volume via a remote focusing strategy. A similar mechanism, based around an adjustable telescope, was previously studied not only as a means of rapidly changing the focal length but also as a method to correct for objective lens spherical aberration.[24] Our scheme is based on counterpropagating acoustic waves in an AO medium, which we have previously used to demonstrate an effective method[25] for spatial dispersion compensation in AO-based MPLSM (AO-MPLSM). In addition, the presented technique relies on continuously changing the frequency of the sound wave in the AO medium, a process known as "chirping." If the change in frequency is linear with time, the resulting angles of deflection at any particular time are similar to those for a cylindrical lens, but the axis of the deflection is also time varying. The use of two AODs, in which the acoustic propagation directions are reversed, removes the time dependence of the deflection angle, and enables a symmetrical cylindrical effect. This idea was demonstrated in a paper by Kaplan et al.[26] to be effective in changing the axial focus, however, in this paper we demonstrate how this system can simultaneously be used for lateral positioning of the focus (which is independent of the axial focal position) and therefore enables full deterministic 3-D scanning.

In addition, we show how this scheme inherently compensates for the decrease in resolution that results when AODs are used with MPLSM. The primary reason for this drop in resolution is spatial dispersion that results from the combination of the frequency-dependent AOD deflection angles with the ultrafast pulses used in MPLSM. The result is a significant increase in the size of the focal volume, which decreases the spatial resolution. We previously showed how, left uncompensated, spatial dispersion can result in up to a 10-fold reduction in the resolution of images obtained via AO-MPLSM and also demonstrated effective compensation schemes using additional diffraction gratings.[25] Here, we demonstrate an equally effective means of compensation, which does not affect our ability to scan axially or laterally.

2 Axial Scanning

2.1 *Theoretical Considerations*

AODs can be viewed as tunable diffraction gratings, where the wavelength of the sound wave propagating through the AO medium, e.g., a tellurium dioxide (TeO_2) crystal, corresponds to the grating constant. Therefore, changing the frequency of the sound wave changes the angle by which the incoming beam is deflected [Fig. 1(a)]. When operated in the Bragg regime, where the Klein and Cook parameter (Q) is[11] much greater than one, the first-order angle of deviation θ can be described by

$$\theta = \frac{\lambda}{\Lambda} = \frac{\lambda f}{v}, \tag{1}$$

where λ is the wavelength of the laser light, Λ is the acoustic wavelength, f is the acoustic frequency (note: throughout this document, frequencies and changes in frequencies are denoted by f, whereas focal lengths and changes in focal length will be denoted by F), and v is the acoustic velocity in the AOD.

If we change the acoustic frequency in time, we can represent both the frequency and the angle of deviation as time-dependent functions $f(t)$ and $\theta(t)$, where Eq. (1) still holds. If we then consider chirped acoustic frequencies [Fig. 1(b)], where $f(t)$ constantly changes, we can define the deflection angle $\theta(x,t)$ at any point x in the aperture of the AOD, as follows:

$$\theta(x,t) = \frac{\lambda}{v} f\left(t - \frac{x}{v}\right), \tag{2}$$

where $x=0$ was, without loss of generality, chosen to be at the center of the AOD aperture, and the positive x direction was chosen to be in the direction of the deflection. We can see from this equation that if we linearly change the acoustic frequency in time (chirp) with a given frequency/time value of α, i.e., let $f(t)=f_{\min}+\alpha t$, where $f_{\min}$ is the lowest acoustic frequency in the bandwidth, $\alpha=(f-f_{\min})/T_{\mathrm{scan}}=\Delta f/T_{\mathrm{scan}}$, and T_{scan} is the duration of the chirp, then the angle of deflection can be defined at any time by

$$\theta(x,t) = \frac{\lambda}{v}(f_{\min} + \alpha t) - \frac{\lambda \alpha}{v^2} x. \tag{3}$$

This equation describes a converging cylindrical lens with a focal length equal to $F=v^2/\lambda\alpha=v^2 T_{\mathrm{scan}}/\lambda\Delta f$, whose central axis of propagation changes from a minimum angle of $\theta = \lambda f_{\min}/v$ at the beginning of the scan to a maximum of θ

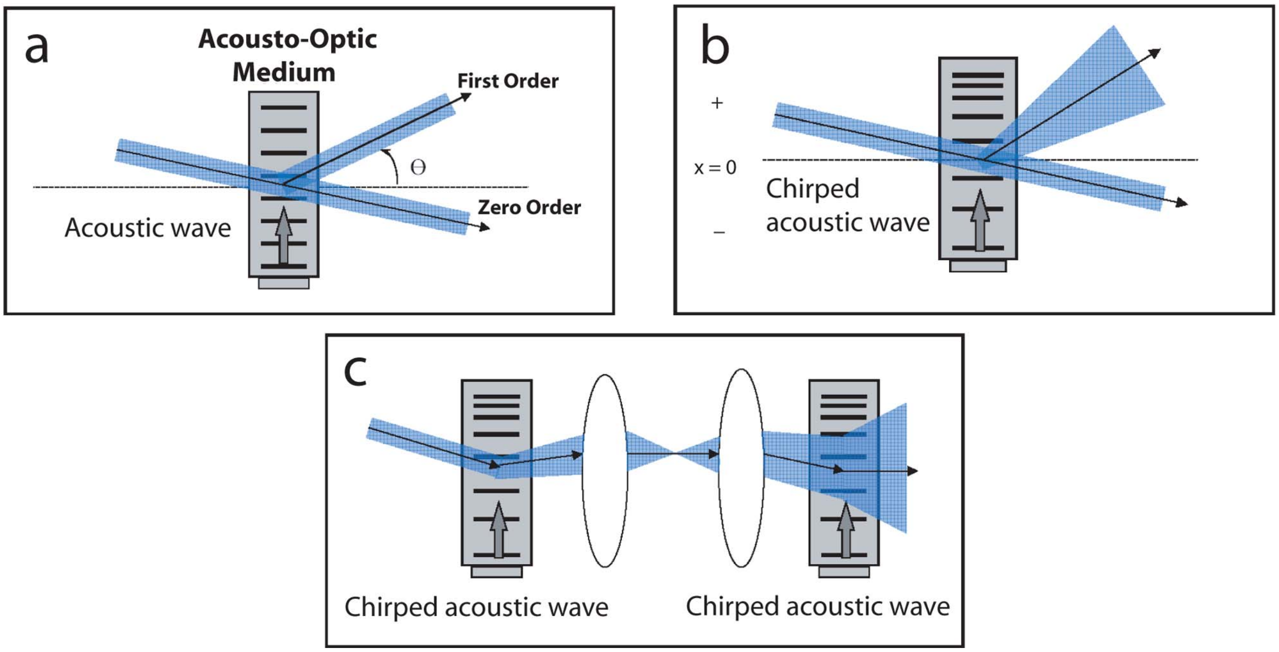

Fig. 1 AOD methods of operation: (a) angular deflection from an AOD operated with a single acoustic frequency, (b) spread of the deflection angles when an AOD is operated with a chirped frequency input, and (c) elimination of the lateral scan by using two AODs and telecentric optics (note that the optical relay makes the second acoustic wave effectively counterpropagating relative to the first).

$=\lambda f/v$ at the end of the scan. Note that we can also make a diverging cylindrical lens [as shown in Fig. 1(b)] by using a negative chirp [i.e., let $f(t)=f-\alpha t$]. Thus, a single AOD with a linearly chirped acoustic signal can be modeled as a cylindrical lens with a time-varying central optical axis.

If we then telecentrically relay the aperture of this AOD to another AOD [Fig. 1(c)], we can describe the total deflection angle by

$$\theta(x,t)=\frac{\lambda}{v}\left[-f_1\left(t+\frac{x}{v}\right)+f_2\left(t-\frac{x}{v}\right)\right], \tag{4}$$

where $f_1(t)$ is the time-dependent acoustic frequency in the first AOD and $f_2(t)$ is the time-dependent acoustic frequency in the second AOD. Note that by reversing the light beam and deviation angles, the optical relay effectively makes the second acoustic wave counterpropagating relative to the first.

If we let the acoustic frequencies $f_1(t)=f_2(t)=f_{\min}+\alpha t$, the total deviation angle can be represented as follows:

$$\theta(x,t)=-\left(2\lambda\frac{\lambda}{v^2}\right)x. \tag{5}$$

This equation now describes a converging cylindrical lens with a central axis of propagation that is time independent. The focal length of this acousto-optic lens (AOL) is

$$F_{\mathrm{AOL,conv}}=\frac{v^2}{2\lambda\alpha}=\frac{v^2T_{\mathrm{scan}}}{2\lambda\Delta f}, \tag{6}$$

in agreement with published results[26] but arranged so that no off-axis deviation is introduced. Thus, for each chirp value α, we get a specific axial focal position. Note that if we use $f_1(t)=f_2(t)=f-\alpha t$ as our chirp frequencies, this results in a diverging cylindrical lens [as shown in Fig. 1(c)] with a focal length of $E_{\mathrm{AOL,div}}=-v^2/2\lambda\alpha=-v^2T_{\mathrm{scan}}/2\lambda\Delta f$.

2.2 *Experimental Evaluation*

2.2.1 *Axial scan*

To demonstrate the effectiveness of the axial scanning scheme, we optically relayed the exit aperture of the AOL to the back focal aperture of an infinity-corrected air objective lens [10×, 0.30-numerical-aperture (NA) Zeiss Plan Neofluar). Therefore, we expect a total focal length equal to

$$F_{\mathrm{total}}=\frac{F_{\mathrm{Obj}}F_{\mathrm{AOL}}}{F_{\mathrm{Obj}}+F_{\mathrm{AOL}}}, \tag{7}$$

where F_{Obj} is the focal length of the objective (~16.5 mm). We imaged and reconstructed a 3-D representation of the scan pattern using the imaging setup described in the following.

Using a continuous wave (cw) argon laser ($\lambda=488$ nm) and two $\mathrm{TeO_2}$ AODs (LS55V, Isomet) with acoustic velocities of $v=619$ m/s, we generated axial scan patterns using a scan time (T_{scan}) of 30 μs and maximal frequency bandwidths of $\Delta f=30$ MHz (giving us a range of α values from -1 to 1 MHz/μs). Specifically, in Fig. 2 we created a five-point axial scan pattern using the cw laser and AO characteristics already described. Figure 2(a) shows the axiolateral projection of the five-point pattern. Figure 2(b) compares predicted [based on Eq. (7)] versus experimentally obtained values for F_{total}.

2.2.2 *Imaging setup*

To acquire our data, we focused the image obtained from an infinity-corrected (32×, 0.6 NA Leitz) air objective lens onto

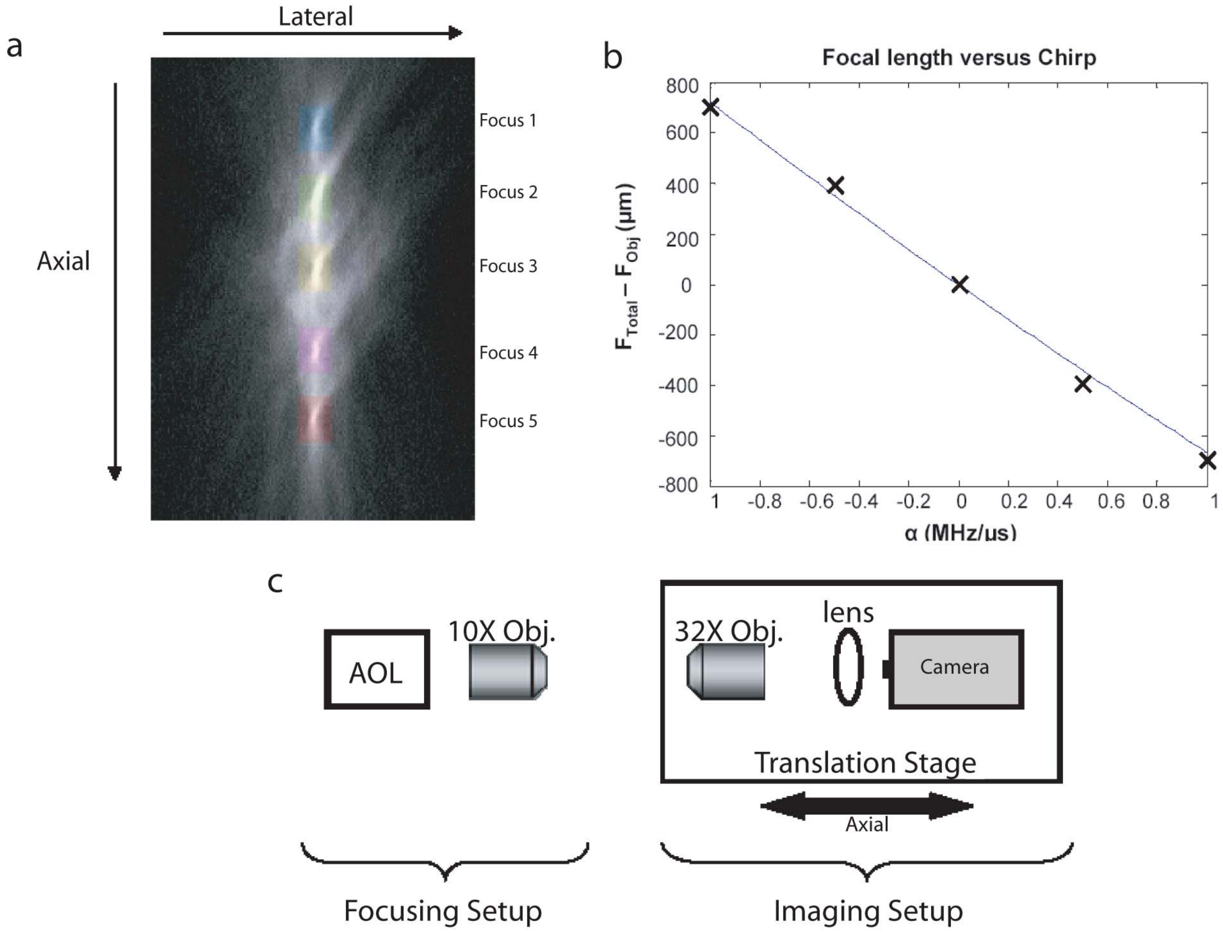

Fig. 2 Axial scan: (a) reconstructed axiolateral projection image of a five-point axial scan pattern (foci 1 to 5) using the 10× Zeiss objective lens mentioned in the text; (b) experimental (marker) and theoretical (line) plot of the total focal length change ($F_{\text{total}} - F_{\text{obj}}$) versus chirp value ($\alpha$) for the AOL scanning scheme, and (c) setup used to acquire images in (a) (for description, see text).

a commercial video camera (WV-1550, Panasonic). Both camera and objective lens were mounted on a translation stage with a resolution of 10 μm in the axial direction [see Fig. 1(c)]. Two-dimensional images were taken at every 10-μm axial step to determine the axial distances of the focal points. Lateral distances were derived from the pixel count. The pixel size was determined by imaging a stage micrometer to assess and normalize for the magnification of the optics. Reconstructed maximum projections were generated using 3-D reconstructing software (Amira 3.0, Template Graphics Software). Intensity plots were generated either by selectively identifying camera pixels onto which focal spots were formed and monitoring the intensity at those pixels as the image stack was acquired or by postacquisition image analysis (MATLAB 7.0, Mathworks).

3 Three-Dimensional Imaging

3.1 *Theoretical Considerations*

If we use the AOD scheme shown in Fig. 1(c) and introduce offsets in the acoustic frequency [i.e., let $f_1(t) = f_{\min} + \alpha t + f_{1\text{offset}}$ and $f_2(t) = f_{\min} + \alpha t + f_{2\text{offset}}$], we find that the total angle of deflection according to Eq. (4) can be described by

$$\theta(x,t) = -\left(2\alpha\frac{\lambda}{v^2}\right)x + (f_{2\text{offset}} - f_{1\text{offset}})\frac{\lambda}{v}. \tag{8}$$

The first part of the right-hand side of this equation is identical to the purely axial case [Eq. (5)] and once again describes a cylindrical lens with a focal length defined by Eq. (6). The second part of the equation defines a time-independent lateral deflection angle

$$\theta_{\text{lateral}} = (f_{2\text{offset}} - f_{1\text{offset}})\frac{\lambda}{v} = \Delta f_{\text{offset}}\frac{\lambda}{v}, \tag{9}$$

which is mathematically independent of the focal length and, therefore, the axial focal position. We can see that when $f_{2\text{offset}} = f_{\max}\{or\, f_{\min}\}$, where $f_{\max}$ is the maximum frequency in the acoustic bandwidth, and $f_{1\text{offset}} = f_{\min}\{f_{\max}\}$, we get a maximal {minimal} scan angle of $\theta_{\text{lateral}} = (\Delta f_{\text{bandwidth}})\lambda/v$ $\{-(\Delta f_{\text{bandwidth}})\lambda/v\}$, where $\Delta f_{\text{bandwidth}}$ is a change in acoustic frequency that is equal to the entire acoustic bandwidth. This gives a total scan range of $\Delta\theta_{\text{lateral}} = 2(\Delta f_{\text{bandwidth}})\lambda/v$. Note that to utilize the maximal lateral scan range, there can be no frequency chirp and thus no axial scanning, a property we further develop in the discussion section.

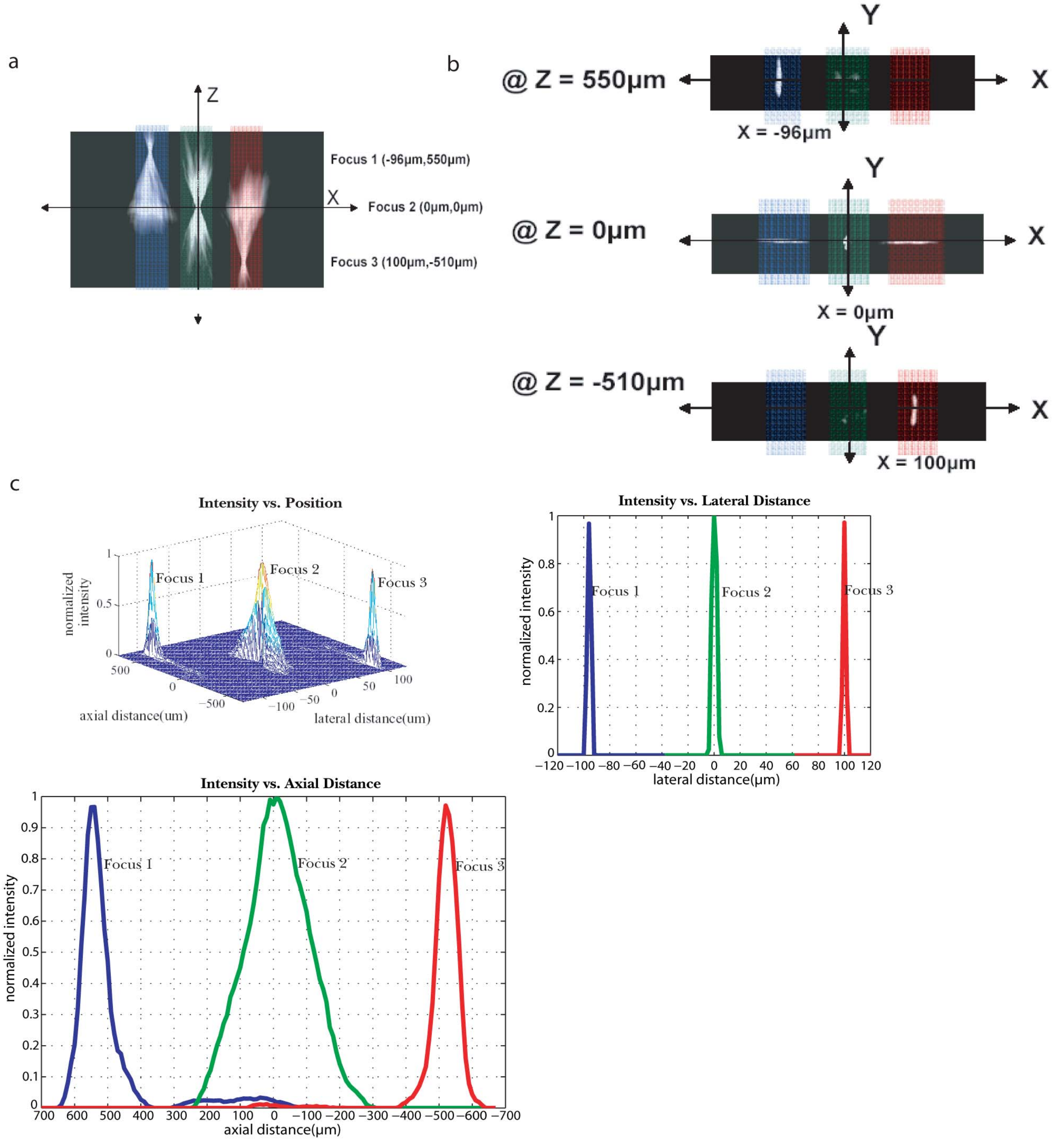

Fig. 3 Axiolateral scan: (a) X to Z maximum projection of a three-point axiolateral scan pattern (foci 1 to 3). The reference position (0,0) is set at the nondeflected and unchirped focus, which is equivalent to the inherent focal position of the objective lens with distances calculated using the intensity plots in (c); (b) X to Y images at particular focus planes showing both the spherical focus at the reference position and the cylindrical focus in the X dimension at the off-center foci, which is a result of the AOL; and (c) intensity plot generated by image analysis of a maximum projection similar to the one in (a). Side projections of the intensity plot show that the lateral and axial spacing between the foci approximately agrees with predictions in Table 1. Note that, as described in the text, due to differences in diffraction efficiency, the center focus (focus 2) is of higher intensity than either side foci and saturates the camera at its peak.

3.2 *Experimental Evaluation*

To demonstrate both axial and lateral scanning, we generated a three-position axiolateral scan pattern (Fig. 3) using the AOL and a 10× objective lens ($F_{\mathrm{obj}}=16.5\,\mathrm{mm}$). We remained for $\sim 30\,\mu\mathrm{s}$ at each focal position, thus enabling us to visit all three spots within the frame rate of the camera.The offset and chirp values used, as well as the predicted [based on Eqs. (6), (7), and (9)] and measured lateral and axial focal positions relative to the inherent focal position of the objective lens (i.e., the focal position if a nondeflected collimated

Table 1 Parameters for Fig. 3.

Focus	Chirp Parameter (α)	Offset Parameter (Δf_{offset})	Predicted Axial Focal Position^a	Measured Axial Focal Position^a	Predicted Lateral Focal Position^a	Measured Lateral Focal Position^a
3	0.75 MHz/μs	7.5 MHz	−504 μm	−510 μm	97.4 μm	100 μm
2	0	0	0	0	0	0
1	−0.75 MHz/μs	−7.5 MHz	537 μm	550 μm	−97.4 μm	−96 μm

Both lateral and axial positions are calculated relative to the inherent focal position of the objective lens, which is equivalent to the position of the second focus since it has neither a chirp nor an offset parameter.

beam is incident on the back focal aperture), are shown in Table 1.

To visualize our scan, we used the imaging setup described in Sec. 2.2 and shown in Fig. 2(c). As we see from the maximum projection image and intensity plots shown in Fig. 3, three foci are laterally and axially distinguishable. Since the image acquisition was not started at a particular location, only relative distances are important. In this regard, the calculated axial (537 and −504 μm) and lateral (±97.4 μm) interfocal distances are close to their measured axial (550 and −510 μm) and lateral (−96 and 100 μm) values. Also, since the differing levels of the AOD diffraction efficiency at each position were not compensated during the acquisition of this image, the inherent objective lens focus has a higher intensity than either off-axis focus. In general, the differing levels of diffraction efficiency can be compensated by utilizing acoustic-wave-generating methods that are capable of modulating the acoustic amplitude in addition to the frequency. However, here, to attain intensity values that were similar, and thus be able to be visualized in the same image, we allowed the objective focus to saturate the camera. As a result, accurate resolution quantification (particularly in regards to comparisons between the on-axis lens focus and the off-axis foci) cannot be attained from this image. The resolution issues of this system, specifically the changes due to the manipulation of the axial focal position, is addressed in the discussion section.

4 Spatial Dispersion Compensation

4.1 *Theoretical Considerations*

As we showed previously,[25] spatial dispersion is a serious limitation when utilizing AODs with MPLSM. It is a direct consequence of the frequency bandwidth found in the ultrafast laser pulses used in MPLSM. The resolution of an AOD is typically defined by the number of resolvable points (NRPs) that can be obtained in the far field, which equals the NRP that can be obtained in the focal plane of an objective lens (if the back focal aperture is filled). This value is defined by the total scan range of the AOD ($\Delta\theta_{\text{scan}}$), which for single AOD operation is defined as

$$\Delta\theta_{\text{scan}} = \frac{\lambda \Delta f_{\text{bandwidth}}}{v}, \tag{10}$$

where $\Delta f_{\text{bandwidth}}$ is the acoustic bandwidth, divided by the minimum spot size. When monochromatic light sources such as cw lasers are used, the minimum spot size is the diffraction limit which, using the Rayleigh criterium, can be approximated by

$$\Delta\theta_{\text{diffraction}} \sim \frac{\lambda}{d}, \tag{11}$$

where d is the effective aperture size of the AOD. However, when light with a significant frequency bandwidth propagates through an AOD, there is an angular spread (spatial dispersion) at any given acoustic frequency that can be described as

$$\Delta\theta_{\text{dispersion}} = \frac{\Delta\lambda f}{v}. \tag{12}$$

When this dispersion is significantly larger than the diffraction limit, it almost exclusively determines the effective spot size. For a tellurium dioxide (TeO_2) AOD with an acoustic velocity $v \sim 620$ m/s and an acoustic bandwidth from 60 to 100 MHz, even at the lowest acoustic frequency, the dispersion angular spread is already ~10 times the size of the diffraction limited angular spread (assuming a beam diameter of ~10 mm and a 100-fs Gaussian pulse with a time bandwidth product of 0.441 and $\lambda \sim 850$ nm, which makes $\Delta\lambda \sim 10.6$ nm). This dispersion decreases the resolution (the number of resolvable spots) by at least a factor of 10.

However, with our 3-D scanning scheme, the lateral scan position is determined by Eq. (9). Thus, the effective bandwidth of the system is from $-\Delta f_{\text{bandwidth}}$ to $+\Delta f_{\text{bandwidth}}$, which for the TeO_2 AOD already described is from −40 to +40 MHz. Using Eq. (12), we see that this implies that at the center frequency, the angular spread due to dispersion is completely eliminated while at extreme scan angles (worst case), the angular spread is only 2/3 of the minimum spread of the single AOD case [see Fig. 4(a)]. However, by utilizing two AODs, we have also effectively doubled our scan range from $\Delta\theta_{\text{scan}}$ to $2\Delta\theta_{\text{scan}}$. Therefore, this scheme results in a minimum improvement in NRP of threefold over the uncompensated case at the extreme scan angles and a progressive increase in NRP toward the center.

4.2 *Experimental Evaluation*

To demonstrate the effect of spatial dispersion, we coupled a multiline laser (main lines of 488 and 514 nm) to a single TeO_2 AOD to simulate the bandwidth of an ultrafast laser that would be used with MPLSM. Using three separate acoustic

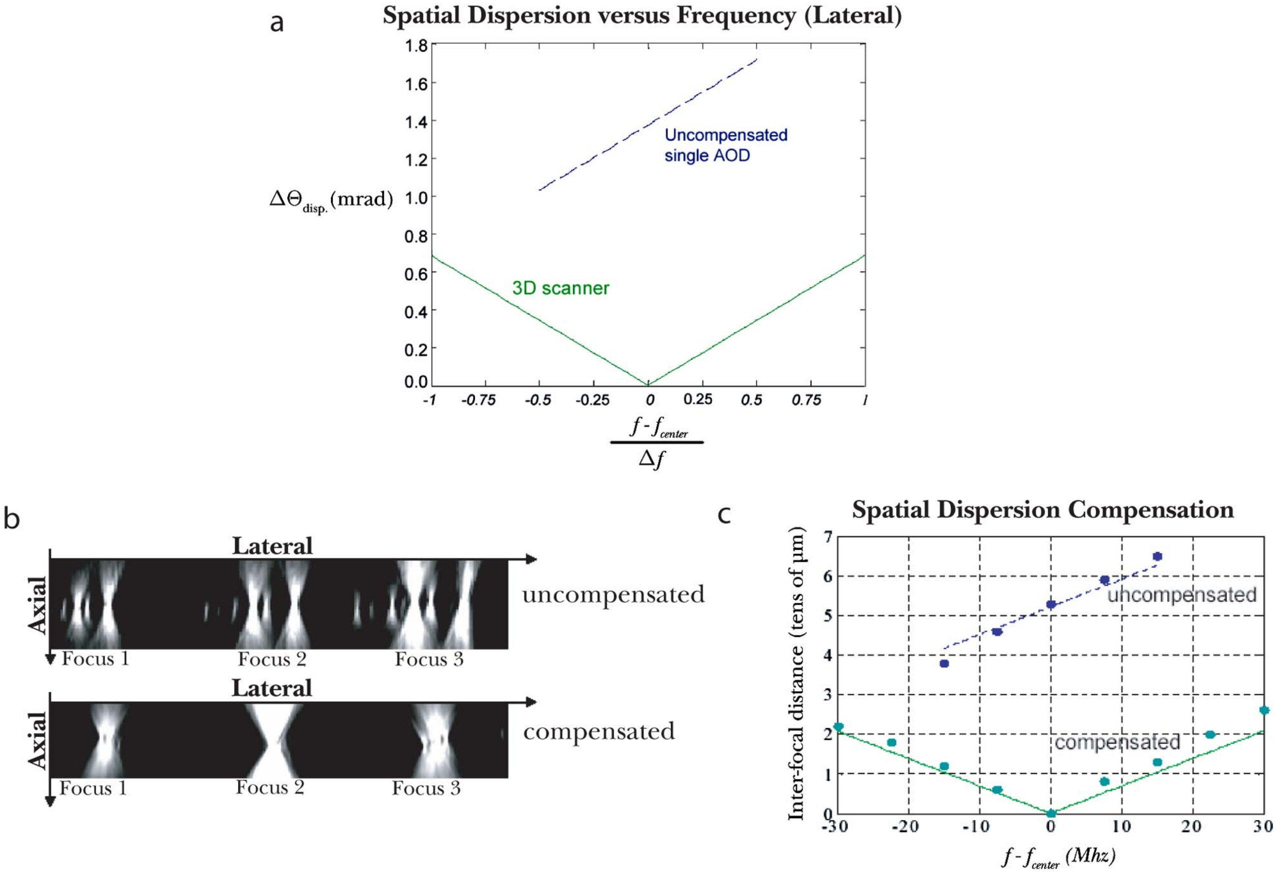

Fig. 4 Spatial dispersion: (a) calculated spatial dispersion (as characterized by $\Delta\Theta_{\mathrm{disp}}$) versus acoustic frequency for the multiphoton scheme described in the text ($\lambda = 850$ nm, $\Delta\lambda = 10.6$ nm), (b) axiolateral projections of a three-point lateral scan pattern with a multiline laser (top) uncompensated scan obtained using a single AOD (bottom) compensated scan obtained using the two AOD scheme, and (c) predicted (lines) and measured values (markers) of spatial dispersion (as characterized by interfocal distances) versus acoustic frequency for both a single AOD (uncompensated) and the two AOD (compensated) scheme when using a multiline laser (main lines of 488 and 514 nm) to mimic the spectral width of an ultrafast laser.

frequencies ($f = 60$, 75, and 90 MHz) and a 10× objective lens ($F_{\mathrm{obj}} = 16.5$ mm), we generated a three-point lateral scan pattern that we imaged and reconstructed using the scheme described in Sec. 2.2 and shown in Fig. 2(c). An axiolateral projection image is shown in Fig. 4(b). At each individual location, the laser lines are spectrally separated in the lateral dimension, which is expected since each wavelength has a specific deviation angle determined from Eq. (1). We then coupled our two-AOD scanner to the multiline laser and rescanned the three positions (using offset acoustic frequency values of $\Delta f_{\mathrm{offset}} = 15$, 0, and -15 MHz, respectively). The result is shown in Fig. 4(b). The separate laser lines perfectly recombine at the center, indicative of complete dispersion compensation. In addition, the spacing between the laser lines at the edges is also significantly decreased. To further quantify this effect, we measured the interfocal spacing between the two major lines of the laser at multiple points in the bandwidth of both the uncompensated single AOD case and the compensated two-AOD case. Using the deviation angles predicted by Eqs. (1) and (9), we can also calculate the separation distance between the foci formed by these two frequencies. Figure 4(c) shows the result of both the calculation (lines) and the measurement (markers). Both show a minimum decrease of $\sim 2/3$ in interfocal distance (and hence dispersion) when using the two-AOD scheme. As mentioned, since we have also doubled our scan range, this indicates a resolution enhancement of at least threefold over the single AOD case.

5 Discussion

Using two AODs, we demonstrated the ability to deterministically scan a cylindrical focus within a 2-D surface. With this scheme, the position of the axial focus can be controlled independently of the lateral focus. This scheme can be adapted to the construction of a 3-D spherical focus scanner by orthogonally cascading two such deflector pairs. While we have demonstrated the basic principles using a multiline cw laser, as mentioned in the introduction, our intended use for this scheme is in multiphoton microscopy. Using the laser parameters ($\lambda \sim 850$ nm), AOD parameters ($\Delta f_{\mathrm{bandwidth}} = 40$ MHz, $v = 619$ m/s), and objective lens parameters (60×, $F_{\mathrm{obj}} \sim 3.33$ mm Nikon) we currently use[8] for 2-D AO-MPLSM, we can calculate our anticipated available axial and lateral scan range [see Figs. 5(a) and 5(b)].

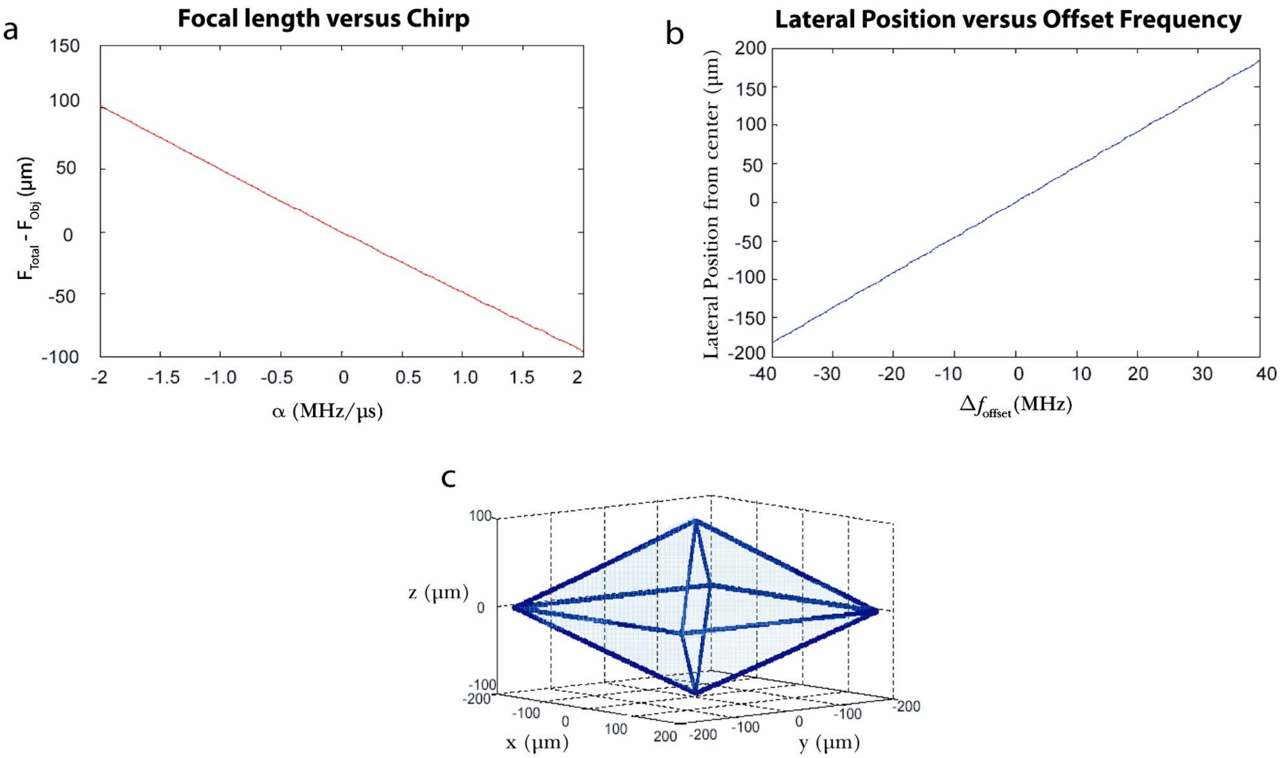

Fig. 5 Anticipated 3-D multiphoton performance parameters, including an ~850-nm wavelength laser, 40-MHz bandwidth TeO_2 AODs, and a 60× objective lens ($F_{obj} \sim 3.33$ mm): (a) axial scan range versus chirp parameter (assuming T_{scan} of 20 μs), (b) lateral scan range versus offset frequency parameter, and (c) outline of the total possible scan range. All accessible points reside within the diamond structure (350×350 ×200 μm).

Note that while the positions of both the lateral and axial focus are mathematically independent of each other, practically they are linked by a finite acoustic bandwidth that must be shared between the two, i.e., $\Delta f_{total} = \Delta f_{lateral} + \Delta f_{axial}$. Thus, as mentioned, the full lateral (axial) scan range is only available when there is no axial (lateral) scan. The overall scan pattern therefore resembles two pyramids attached to each other at their bases [see Fig. 5(c)]. Also, note that the lateral and axial resolutions are not equivalent. To show this, we examine the equations for both lateral and axial resolution. The lateral resolution attainable by the proposed 3-D scanner was already described and can be represented as the total scan range divided by the minimum spot size. Therefore, if we ignore spatial dispersion, the NRP can be expressed as

$$\mathrm{NRP}_{\mathrm{lateral}} = \frac{(\lambda \Delta f_{\mathrm{lateral}}/v)}{\dfrac{\lambda}{d}} = \frac{d}{v} \Delta f_{\mathrm{lateral}}, \tag{13}$$

where d represents the size of the AOD aperture. Similarly, in the axial dimension, the NRP, according to Kaplan et al.,[26] can be expressed as

$$\mathrm{NRP}_{\mathrm{axial}} = \left(\frac{4\pi}{\eta} \right) \frac{(d/v)^2}{T_{\mathrm{scan}}} \Delta f_{\mathrm{axial}}, \tag{14}$$

where η is a constant that depends on the beam shape (~7 for a constant intensity laser beam).

Note that both of the preceding equations assume a constant lateral and axial resolution throughout the entire scan pattern, however, we have already described in Sec. 4 how the resolution will change as a result of spatial dispersion if used in MPLSM. Another source of resolution reduction results from an effective drop in NA, which is a quantitative measurement of the resolution of the system, at axial distances further than the objective plane. We can calculate the smallest NA, which will occur at the farthest axial point, as

$$\mathrm{NA}_{\min} = n(\sin \theta_{\min}) = n \frac{D}{2[(W_d + \Delta F)^2 + (D/2)^2]^{1/2}}, \tag{15}$$

where W_d is the working distance of the objective lens, D is the diameter of the front lens of the objective, and $\Delta F = F_{\mathrm{total}} - F_{\mathrm{obj}}$ is the distance between the farthest axial focal position and the objective focal plane. For a 60× water immersion lens with an NA of 1.0 and a working distance of 2.0 mm, if we had a ΔF of 100 μm, then the $\mathrm{NA}_{\min}$ is 0.98. This implies a 2% maximum increase in lateral spot size and a 4% maximum increase in axial spot size.

Another particular resolution concern when imaging optically thick biological specimens is spherical aberration, which results from distortions in the light wavefront as it passes thorough the heterogeneous refractive index environment. While we have not specifically addressed this issue, a study by Kam et al.,[24] which used a remote telescoping method similar to ours but based around a classical telescope, showed that in addition to axial scanning, this method could also be used to compensate for spherical aberration at different focusing depths, but only if used in conjunction with conventional objective lens focusing. However, this study also showed that using the remote focusing method by itself enabled the axial scanning of relatively large distances ($\sim 50\ \mu$m), while maintaining acceptable levels of aberration. Even though this distance is less than our anticipated working axial scan range ($\sim 200\ \mu$m), it is quite sufficient for several interesting neuroscience experiments. In fact, we estimate that only a fraction of the entire scan volume presented in Fig. 5(c) is required for the experiments we have planned (i.e., a volume of $100 \times 100 \times 100\ \mu$m).

Note that while the resolution changes are important, this scanning scheme is being developed for functional imaging of neurons, where small processes, such as oblique dendrites and spines, are relatively sparse. Therefore, the resolution issues already discussed, and those that will be difficult to determine until a full 3-D system containing four AODs is constructed, are not as crucial as they would be in structural imaging, specifically since, for this application, temporal resolution is of particularly high importance.

While we developed this scheme for functional multiphoton microscopy, we are aware that there are several issues that are not dealt with in this manuscript that are important for the application of this 3-D AOD-based scanning scheme to MPLSM, such as potential power losses. One significant source of potential incident power loss will be from temporal dispersion. Our lab previously discussed[25] the effect of temporal dispersion caused by using AODs in MPLSM and also implemented methods of compensating for it, which include using a prechirper[25] or increasing the laser pulse duration[8] to intermediate values (~ 400 fs). This last compensation method has the advantage of simultaneously reducing spatial dispersion and is quite possibly the best mechanism for reducing the estimated $60{,}000\ \text{fs}^2$ of group velocity dispersion (GVD) that will be introduced by four AODs since, even with a compacted design, a prechirper-based mechanism would require extensive space on an optical table. Another source of incident power loss will be from the estimated 50% diffraction efficiency of each AOD (note that since every AOD cannot be adjusted for maximum efficiency, this reduces the normal peak diffraction efficiency value of 70%). Thus, ignoring any other losses in the path, only $\sim 6.25\%$ of the incident power will reach the preparation. Most of these power losses can be compensated by increasing the output power of the laser, if sufficient power is available. For this reason, we anticipate that the implementation of this scheme will require an ultrafast laser with an average output power greater than 2 W.

Another important possible limitation for the implementation of this scheme is that unlike in the 2-D case, there is a limit to the amount of time we can remain at certain positions in 3-D space. This limitation is due to the finite acoustic bandwidth of the AODs. Using Eq. (6) and given a fixed bandwidth Δf_{axial}, we see that the farther we want to displace our focal point in either the positive or negative axial direction, the shorter our scan time (T_{scan}) must be, with a limit set at the aperture time of the AOD. Therefore the amount of time we can remain at a given axial position is the difference between the T_{scan} value required to attain that position and the aperture time of the AOD. After this time has elapsed, we must wait another aperture time before resuming scanning. Our T_{scan} value gradually increases toward the focal plane of the objective, at which point it is infinite and we can remain at any lateral position.

In conclusion, note the advantages that a functional imaging system utilizing fast 3-D scanning would provide, particularly in the field of experimental neuroscience. These include experiments involving the 3-D monitoring of physiological signals along complex dendritic structures in optically thick tissue, such as brain slices and even intact brains, which have thus far been unattainable. In this paper, we developed a scheme that by effectively and simultaneously laterally and axially scanning enables this possibility for the first time. In addition, we tailored this technique for MPLSM, where we have shown that it would inherently compensate for spatial dispersion, which has limited the use of AODs in MPLSM. Thus, it has a strong potential application in the field of functional neuronal imaging.

Acknowledgments

We thank Dr. Vivek Bansal and Brad Losavio for their comments on this manuscript and their invaluable help throughout this project. We also appreciate the technical advice of Dr. Vijay Iyer and Dr. Saumil Patel during the early stages of this project. This work was supported by grants from the National Institutes of Health (NIH) and the National Science Foundation (NSF) to PS.

References

1. W. Zipfel, R. Williams, and W. Webb, "Nonlinear magic: multiphoton microscopy in the biosciences," *Nat. Biotechnol.* **21**, 1369–1377 (2003).
2. R. H. Christie, B. J. Bacskai, W. R. Zipfel, R. M. William, S. T. Kajdasz, W. W. Webb, and B. T. Hyman, "Growth arrest of individual senile plaques in a model of Alzheimer's disease observed by in vivo multiphoton microscopy," *J. Neurosci.* **21**, 858–864 (2001).
3. B. J. Bacskai, S. T. Kajdasz, R. H. Christie, C. Carter, D. Games, P. Seubert, D. Schenk, and B. T. Hyman, "Imaging of amyloid-beta deposits in brains of living mice permits direct observation of clearance of plaques with immunotherapy," *Nat. Med.* **7**, 864–868 (2001).
4. K. Svoboda, D. W. Tank, and W. Denk, "Direct measurement of coupling between dendritic spines and shafts," *Science* **272**, 716–719 (1996).
5. J. Deng and A. Dunaevsky, "Dynamics of dendritic spines and their afferent terminals: spines are more motile than presynaptic boutons," *Dev. Biol.* **277**, 366–377 (2005).
6. R. Yuste and W. Denk, "Dendritic spines as basic functional units of neuronal integration," *Nature (London)* **375**, 662–664 (1995).
7. R. Yasuda, E. A. Nimchinsky, V. Scheuss, T. A. Pologruto, T. G. Oertner, B. L. Sabitini, and K. Svoboda, "Imaging calcium concentration dynamics in small neuronal compartments," *Science* **STKE 219**, 15 (2004).
8. V. Iyer, T. Hoogland, B. Losavio, R. Fink, R. Gaddi, S. Patel, S. A. Larson, and P. Saggau, "Acousto-optic multiphoton laser scanning microscopy (AO-MPLSM) for structural and functional imaging in living brain slices," *Proc. SPIE* **5700**, 90–102 (2005).
9. V. Bansal, S. Patel, and P. Saggau, "High-speed confocal laser scanning microscopy using acousto-optic deflectors and a digital micromirror device," *Proc. SPIE* **5324**, 47–54 (2004).
10. A. Bullen, S. S. Patel, and P. Saggau, "High-speed, random access fluorescence microscopy: I. High resolution optical recording with voltage-sensitive dyes and ion indicators," *Biophys. J.* **73**, 477–491 (1997).
11. M. Gottlieb, C. L. M. Ireland, and J. M. Ley, *Electro-Optic and Acousto-Optic Scanning and Deflection*, Marcel Dekker, New York (1983).
12. J. Xu and R. Stroud, *Acousto-Optic Devices: Principles, Design, and*

Applications, John Wiley and Sons, New York (1992).

13. H. McNally, B. Rajwa, J. Sturgis, and J. P. Robinson, "Comparative three-dimensional imaging of living neurons with confocal and atomic force microscopy," *J. Neurol. Meth.* **142**, 177–184 (2005).
14. D. B. Edelman and E. W. Keefer, "A cultural renaissance: in vitro cell biology embraces three-dimensional context," *Exp. Neurol.* **192**, 1–6 (2005).
15. N. Sugiura and S. Morita, "Variable-focus liquid-filled optical lens," *Appl. Opt.* **32**, 4181–4186 (1993).
16. D. Zhang, V. Lien, Y. Berdichevsky, J. Choi, and Y. Lo, "Fluidic adaptive lens with high focal length tunability," *Appl. Phys. Lett.* **82**(19), 3171–3172 (2003).
17. H. Oku, K. Hashimoto, and M. Ishikawa, "Variable-focus lens with 1-kHz bandwidth," *Opt. Express* **12**(10), 2138–2149 (2004).
18. H. Ren, Y. H. Fan, S. Gauza, and S. T. Wu, "Tunable-focus cylindrical liquid crystal lens," *Jpn. J. Appl. Phys., Part 1* **43**(2), 652–653 (2004).
19. H. Ren, Y. H. Fan, S. Gauza, and S. T. Wu, "Tunable-focus flat liquid crystal spherical lens," *Appl. Phys. Lett.* **84**(23), 4789–4791 (2004).
20. L. G. Commander, S. E. Day, and D. R. Selviah, "Variable focus length microlenses," *Opt. Commun.* **177**, 157–170 (2000).
21. T. Shibaguchi and H. Funato, "Lead-lanthanum zirconate-titanate (PLZT) electrooptic variable focal-length lens with stripe electrodes," *Jpn. J. Appl. Phys., Part 1* **31**, 3196–3200 (1992).
22. L. Zhu, P. C. Sun, and Y. Fainman, "Aberration-free dynamic focusing with a multichannel micromachined membrane deformable mirror," *Appl. Opt.* **38**(25), 5350–5354 (1999).
23. G. Reddy and P. Saggau, "Fast three-dimensional laser scanning using acousto-optic deflectors," *Proc. SPIE* **5700**, 311–318 (2005).
24. Z. Kam, D. A. Agard, and J. W. Sedat, "Three-dimensional microscopy in thick biological samples: a fresh approach for adjusting focus and correcting spherical aberration," *Bioimaging* **5**, 40–49 (1997).
25. V. Iyer, B. Losavio, and P. Saggau, "Compensation of spatial and temporal dispersion for acousto-optic multiphoton-laser scanning microscopy," *J. Biomed. Opt.* **8**(3), 460–471 (2003).
26. A. Kaplan, N. Friedman, and N. Davidson, "Acousto-optic lens with very fast focus scanning," *Opt. Lett.* **26**(14), 1078–1080 (2001).